Mechanistic Insight into pH-Driven Phase Transition of Lipid Nanoparticles

Marius F.W. Trollmann[1,2] and Rainer A. Böckmann[1,2,3*]

[1]Computational Biology, Department of Biology, Friedrich-Alexander-Universität Erlangen-Nürnberg, Erlangen, Germany.
[2]Erlangen National High-Perfomance Computing Center (NHR@FAU), Erlangen, Germany.
[3]FAU Profile Center Immunomedicine (FAU I-MED), Erlangen, Germany.
[*]rainer.boeckmann@fau.de.

*Corresponding author. E-mail: rainer.boeckmann@fau.de;
Contributing authors: marius.trollmann@fau.de;

Abstract

Lipid nanoparticles (LNPs) are essential delivery vehicles in mRNA-based vaccines, with their functionality largely governed by aminolipids. At low pH, protonated aminolipids facilitate efficient mRNA encapsulation, while their deprotonation at physiological pH drives LNP remodeling into a stable spherical structure, potentially aiding mRNA release during endosomal re-protonation and concomitant restructuring at low pH.

Our study uncovers the pH-dependent phase transition of the *Comirnaty* lipid formulation at the molecular scale, highlighting the intricate interplay between lipid reorganization and aminolipid protonation. We observe a substantial shift in the aminolipid pK_a, from 7-8 at the LNP surface to below 4 within the hydrophobic LNP core, resulting in an overall apparent pK_a of the lipid nanoparticle of 6.3. The pH-dependent protonation significantly affects the aminolipid's localization, with protonated aminolipids enriched in vicinity of the mRNA and at the LNP surface at neutral pH. The lipid monolayer covering LNPs at neutral pH comprises cholesterol (60–65%), helper phospholipids (20–25%), PEGylated lipids (5%), and a mix of protonated and deprotonated aminolipids (5–10%). These findings provide mechanistic insights into aminolipids behavior in LNPs, offering a foundation for optimizing LNP design to enhance stability, tunable pH responses, and therapeutic efficacy.

Lipid nanoparticles (LNPs) have become a well-established platform for delivering polynucleotides such as mRNA and siRNA, as demonstrated by therapeutic products such as Onpattro [1] and SARS-CoV-2 vaccines [2–4]. This delivery technology holds significant promise for future vaccines targeting cancers [5, 6] and infectious diseases, e.g., malaria [7, 8]. For instance, BioNTech has developed three mRNA-based vaccines (BNT142, BNT152, and BNT153), all currently in phase 1 clinical trials (NCT05262530, NCT04710043) for treating solid tumors. Another LNP-based vaccine, NBF-006 by Nitto BioPharma, is also undergoing phase 1 trials (NCT03819387) for non-small cell lung, pancreatic, and colorectal cancers.

In LNP formulations, the lipid components play a crucial role in determining the immunogenicity and therapeutic efficacy of the delivered nucleotides [9]. Most LNPs consist of four key components [1, 10]: (1) ionizable aminolipids, capable of changing their protonation state under physiological conditions [11]; (2) PEGylated lipids, which control particle size [12, 13], prevent aggregation [13, 14], and enhance circulation time in the body after administration [15, 16]; (3) cholesterol; and (4) helper phospholipids like 1,2-Distearoyl-sn-glycero-3-phosphocholine (DSPC), which improve stability and transfection efficiency of the LNPs [13, 17]. Together, these lipids encapsulate and protect mRNA from environmental degradation [10, 18], enabling enhanced transfection compared to unencapsulated mRNA [9].

Two key properties of ionizable aminolipids influencing transfection efficiency are their pK_a and molecular shape. The pK_a dictates the lipid's protonation state relative to environmental pH. For example, Carrasco *et al.* [11] reported that LNP pK_a values typically range from 6 to 7, aligning with the acidic environments of the early (pH 6.5) and late endosomes (pH 5.5) [19]. This suggests that ionizable aminolipids trigger the release of nucleic acids in response to the acidic endosomal environment. Protonation of aminolipids enhances interactions with the negatively charged endosomal membrane, leading to membrane disruption and facilitating the release of LNP cargo, potentially via the formation of an H_{II}-phase [20, 21]. This process is supported by the conical molecular shapes of aminolipids like D-Lin-MC3-DMA ((6Z,9Z,28Z,31Z)-6,9,28,31-Heptatriacontatetraen-19-yl 4-(dimethylamino)butanoate) used in Onpattro [1], SM-102 (9-Heptadecanyl 8-(2-hydroxyethyl)[6-oxo-6-(undecyloxy)hexyl]aminooctanoate) used in *Elasomeran* by Moderna [3], or ALC-0315 ([(4-Hydroxybutyl)imino]di-6,1-hexanediyl bis(2-hexyldecanoate)) used in Pfizer-BioNTech's *Comirnaty* [2]. Notably, the pK_a of LNPs is significantly lower than the *intrinsic* pK_a of isolated, solvated aminolipids, which typically ranges between 8.5 and 9.5 [11]. The reason for this shift by approximately 3 units in pK_a and, related, the pH-dependent charge distribution in LNPs remains poorly understood.

Recent advances in molecular dynamics (MD) simulations have provided new insights into the structure, dynamics, and pH-dependent remodeling of LNPs. These studies usually focus on small systems like periodic membrane patches [18, 22–26] or LNP core-like systems [27] to maximize computational efficiency. Early coarse-grained simulations by Leung *et al.* [28] revealed periodic aqueous compartments within siRNA LNPs. More recently, Trollmann and Böckmann constructed an atomistic model of the mRNA-devoid *Comirnaty* LNP, suggesting an oil-like core consisting of aminolipids

and cholesterol that is surrounded by a monolayer of DSPC, cholesterol, aminolipids, and PEGs, with an approximate diameter of 35 nm [18]. Based on the characteristics of simulations including lipids and mRNA strands in a similar N/P (nitrogen-to-phosphate) ratio as in *Comirnaty*, a diameter of the *Comirnaty* vaccine LNP of ≈ 50 nm was suggested, and recently corroborated in a small-angle X-ray scattering (SAXS) study [29]. MD simulations have also demonstrated lipid hexagonal phase formation around RNA under acidic conditions [30], while RNA is expelled from LNP-like structures at neutral pH [18, 30]. These studies, along with methodological advances such as the MARTINI (v3.0) coarse-grained force field extension to lipid nanoparticles [31], have improved the modeling of ionizable lipids, simplifying the generation of topologies for both known and novel aminolipids. MD simulations also enabled first studies of LNP fusion with model membranes. For example, Čechová *et al.* demonstrated enhanced fusogenicity of lipid nanodroplets with lipid bilayers at neutral pH compared to acidic conditions [26]. Kjølbye *et al.* further quantified the fusion barrier between LNP-mimetic bilayers and mammalian model membranes at low pH, highlighting the critical role of anionic endosomal lipids in these interactions [31].

Despite these advances, most MD simulations of aminolipids assume fixed protonation states, overlooking the dynamic behavior of titratable groups. To address this limitation, Tesei *et al.* [32] recently employed Monte Carlo simulations to study aminolipid protonation dynamics in simplified systems. Their results suggest that the protonation state of aminolipids depends on their shape and headgroup chemistry. Differently, atomistic MD simulations by Grava *et al.* [25] used fixed protonation states for D-Lin-MC3-DMA in lipid monolayers; The authors developed a self-consistent scheme to determine the protonation degree of the aminolipids by comparing the packing of the lipids in simulations with experimental total reflection x-ray scattering and x-ray fluorescence data. This approach revealed a shift in the apparent pK_a indicating a lower degree of protonation than predicted by the intrinsic pK_a of the aminolipid. However, atomistic-level investigations of pH-dependent charge distributions in realistic LNP environments remain sparse.

In this study, we investigate the protonation behavior and charge distribution of aminolipids in LNP-like systems at atomistic resolution. Using a constant-pH molecular dynamics (CpHMD) approach based on λ-dynamics [33, 34], we allow titratable sites to dynamically adjust their protonation states in response to local environmental factors and long-range electrostatic interactions. The recent implementation of constant-pH MD in Gromacs [34] enables accurate modeling of interactions among hundreds of titratable sites, providing unprecedented insight into these complex systems. In particular, we parameterized this method for ALC-0315, the aminolipid used in the *Comirnaty* vaccine [2], to investigate its behavior within complex membrane compositions under varying pH conditions and in the absence and presence of mRNA. Our findings highlight a notable shift in the pK_a of ALC-0315 when incorporated into a realistic lipid environment. At neutral pH, a significant fraction of protonated aminolipids was observed within the LNP surface layer, emphasizing their critical role in the biophysical properties and functionality of the nanoparticle.

Results

The pH-dependent structural organization, core and shell lipid compositions, and the distribution of protonated and deprotonated aminolipids, along with their related pK_a values (Fig. 1), were analyzed from unbiased all-atom constant-pH MD simulations of LNP-mimetic membrane patches reflecting the lipid composition of *Comirnaty* LNPs. The initial configuration consisted of all aminolipids in their protonated state. At this low-pH starting condition, classical MD simulations revealed the spontaneous self-aggregation of lipids into a bilayer membrane on the sub-microsecond timescale (see Fig. 2a, left panel) [18].

Modeling the intrinsic pK_a of the aminolipid ALC-0315. The parameterization of ALC-0315 was validated using CpHMD simulations of a single aminolipid solvated in water at physiological salt conditions (150 mM Na^+Cl^-) across a pH range of 5 to 12 (Tab. 1, system C). These simulations comprised 14 distinct pH conditions, each with 9 replicas, for a total simulation time of 0.7 μs per replica. Any significant deviation of the numerically derived pK_a from the pre-defined reference value would suggest either insufficient sampling during titration or an inadequate estimation of the protonation free energy $V^{MM}(\lambda)$ via thermodynamic integration (see Methods for parameterization details). The intrinsic pK_a of 9.29 ± 0.02 was determined by fitting the Henderson-Hasselbalch equation (Eq. 4) to the mean aminolipid deprotonation fraction (S^{deprot}), as shown in Fig. 1a. This value closely matches the reference pK_a of 9.26 [35], indicating both sufficient sampling and accurate parameterization of the protonation behavior of ALC-0315.

***Comirnaty*-formulation lowers the apparent pK_a of ALC-0315.** The protonation behavior of aminolipids within the BioNTech/Pfizer LNP formulation was characterized based on microsecond CpHMD simulations of periodic membrane patches for different pH values (systems D, E, F^1-F^6, see Tab. 1 and Fig. 2a).
The initial structure for all CpHMD simulations was based on a lipid bilayer obtained from classical MD at acidic pH, with all aminolipids protonated [18] (similar to Fig. 2a, pH 5.17). Systems F^1-F^6 (pH 6-11) were quadruplicated with respect to the initial low-pH structure (systems D, E) to allow for large-scale phase transitions.

Fig. 1b illustrates, over a representative time interval and aminolipid, how the λ-coordinate, which defines the protonation state of an aminolipid ($\lambda = 0$ for protonated, $\lambda = 1$ for deprotonated), is influenced by its position within the LNP-mimetic membrane. When the aminolipid transitions from the solvent-membrane interface to the bulk lipid phase (e.g., between 20 ns and 30 ns in Fig. 1b), it rapidly deprotonates. Conversely, upon returning to the polar membrane interface (e.g., between 60 ns and 70 ns in Fig. 1b), it promptly protonates. These (de-)protonation events occur on a timescale of just a few nanoseconds, demonstrating the ability of aminolipids to swiftly adapt their protonation state in response to local environmental changes. At the same time, the timescale of protonation adjustments is sufficiently slow to allow for changes in the aminolipid's membrane localization.

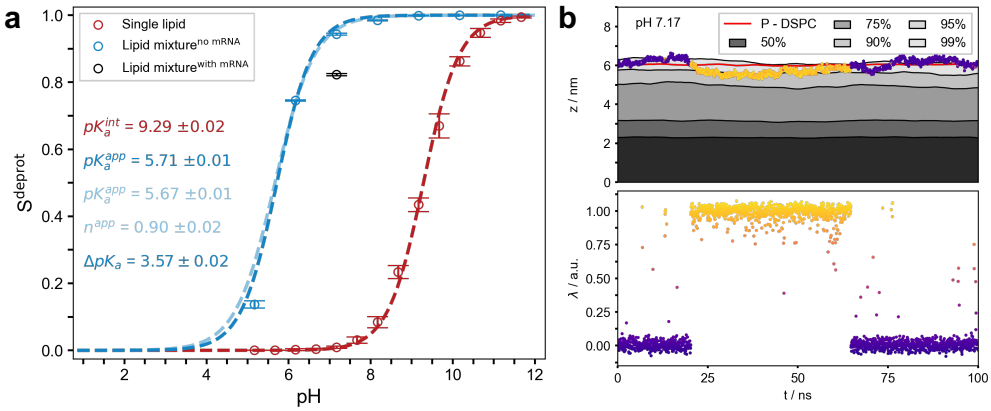

Fig. 1 Protonation characteristics of aminolipids. a Titration curves of ALC-0315 solvated in water (*red*) and within a LNP-mimetic based on the *Comirnaty* formulation (*blue* without mRNA, and *black* data point with mRNA, Structure 1). Circles indicate the fraction of deprotonated lipids (S^{deprot}) at each pH. Dashed lines represent fits using the (generalized) Henderson-Hasselbalch equation, used to determine the intrinsic and apparent $\mathrm{pK_a}$ values and the degree of cooperativity. Fit results of the generalized Henderson-Hasselbalch equation are displayed with higher transparency. Error bars for S^{deprot} represent the standard error of the mean, either calculated via block averaging (*blue*) [36] or from replica simulations (*red*). Errors for the fit parameters correspond to one standard deviation [37]. Averages were calculated after S^{deprot} values reached equilibrium (Supplementary Fig. 6). **b** The upper panel shows the z-coordinate of the nitrogen atom in a single aminolipid within the LNP-mimetic over time, colored by its λ-coordinate (*blue*, ≈ 0; *yellow*, ≈ 1). Bulk aminolipids are represented by the $50\% - 99\%$ quantiles of their nitrogen z-coordinates, smoothed with a 5 ns running average. The lower panel illustrates the λ-coordinate over the same period using the same color scheme. Spatial coordinates are given relative to the membrane center, defined by the median position of the phosphor atoms in DSPC.

The *apparent* $\mathrm{pK_a}$ of aminolipids within the *Comirnaty* lipid formulation was derived by fitting the Henderson-Hasselbalch equation (see Eq. 4) to the fraction of deprotonated aminolipids in the LNP-mimetic membrane patch (S^{deprot}, Fig. 1a).

The lipid environment induces a significant shift in the apparent $\mathrm{pK_a}$ by ≈ 3.5 units to 5.71 ± 0.01 with respect to the intrinsic $\mathrm{pK_a}$ of 9.29 (Fig. 1a), corresponding to a protonation equilibrium shift of approximately 21 kJ/mol. This value aligns closely with the experimentally determined $\mathrm{pK_a}$ of 6.09 for *Comirnaty* LNPs obtained using a fluorescence-based assay with 2-(p-toluidino)-6-napthalene sulfonic acid (TNS) [38], with a deviation of approximately 2 kJ/mol.
Incorporating cooperativity into the analysis yields a comparable $\mathrm{pK_a}$: By assuming aminolipids behave similarly to polyelectrolytes [11], fitting the *generalized* Henderson-Hasselbalch equation (Eq. 5) [39] results in an apparent $\mathrm{pK_a}$ of 5.67 ± 0.01 and a cooperativity parameter $n = 0.90 \pm 0.02$. The value of $n < 1$ indicates anti-cooperativity, where deprotonation of one aminolipid reduces the likelihood of neighboring aminolipid deprotonation, and vice versa for protonation. This anti-cooperative behavior is consistent with titration curves from ζ-potential measurements of various LNP compositions by Carrasco *et al.* [11].

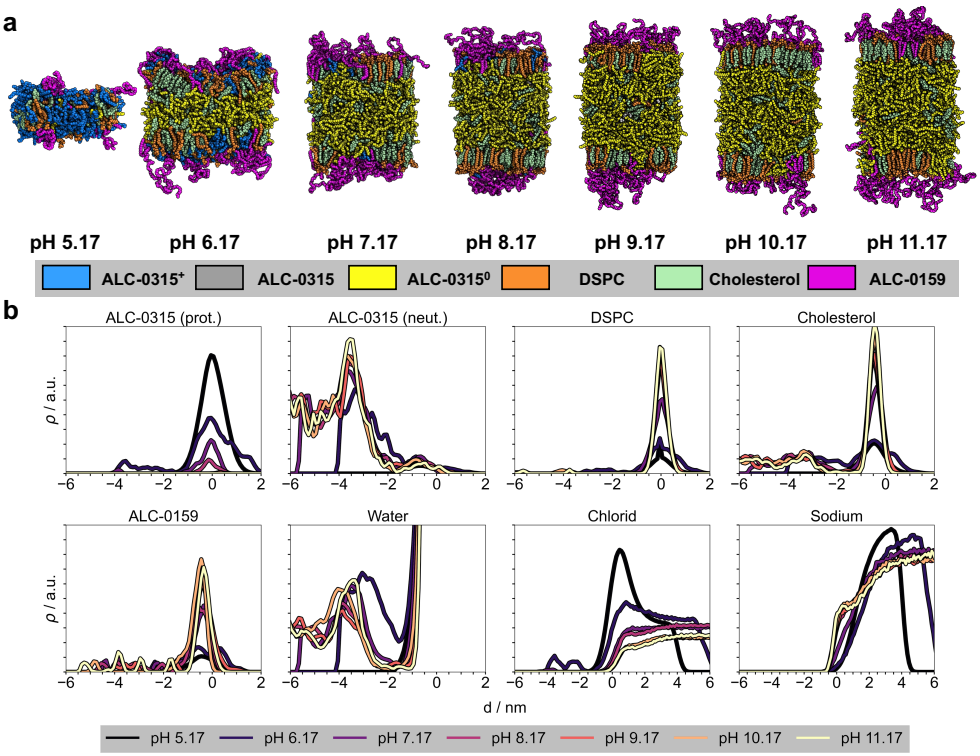

Fig. 2 pH-dependent LNP phases. a Snapshots of the LNP composition at different pH values. As the pH increases, the aminolipids transition from a protonated state (*blue*) to a deprotonated state (*yellow*), forming a hydrophobic core together with cholesterol (*palegreen*). DSPC (*orange*), ALC-0159 (*hotpink*), and the remaining cholesterol (*green*) accumulate at the boundaries with the solvent phase. ALC-0315 without a specific protonation state ($0.2 \leq \lambda \leq 0.8$) is shown in *gray*. **b** Average mass densities for all molecule types relative to the membrane surface, defined by the median z-position of the phosphorus atoms in DSPC in one leaflet, at different pH levels. The density curves were calculated using the following atoms for each molecule type: nitrogen for ALC-0315, phosphorus for DSPC, oxygen for cholesterol, nitrogen for ALC-0159, and oxygen for water. Density curves represent averages taken after equilibration of box vectors (for pH 5, 10, and 11) or over the final 100 – 200 ns of the simulation for other pH values (Supplementary Fig. 5).

pH-driven phase transition in *Comirnaty* LNP formulation. The structural and phase behavior of the *Comirnaty* LNP formulation was investigated using CpHMD simulations across a pH range of 5 to 11. Increasing pH reduced the proportion of protonated aminolipids from 88% at pH 5 to 1% at pH 11 (Fig. 1a). This shift profoundly influenced the molecular organization of the lipid membrane. At pH 5, the bilayer structure remained stable throughout microsecond-long CpHMD simulations (Fig. 2a, protonated aminolipids in *blue*, deprotonated in *yellow*), consistent with previous findings using fully protonated aminolipids [18]. At pH 11, the bilayer underwent a phase transition, stabilizing after 7.5 μs of all-atom simulation into a LNP-mimetic phase (Supplementary Fig. 5; phase transition for system at pH 6 and pH 7 not fully developed after 7-8 μs). This phase featured a hydrophobic core composed of $\approx$ 70%

aminolipids and ≈ 30% cholesterol (Fig. 3), flanked by lipid monolayers. The cholesterol concentration in the monolayers increased significantly from ≈ 40% at pH 5 to ≈ 65% at pH 11 (Fig. 3), close to the cholesterol solubility limit in phospholipid membranes [40]. This behavior aligns with classical MD simulations with deprotonated aminolipids [18]. The monolayer shell at pH 11 also incorporated all DSPC helper lipids (24% of monolayer lipids/cholesterol), PEGylated lipids (5%), and 5% deprotonated aminolipids, illustrating a significant reorganization driven by pH. The CpHMD

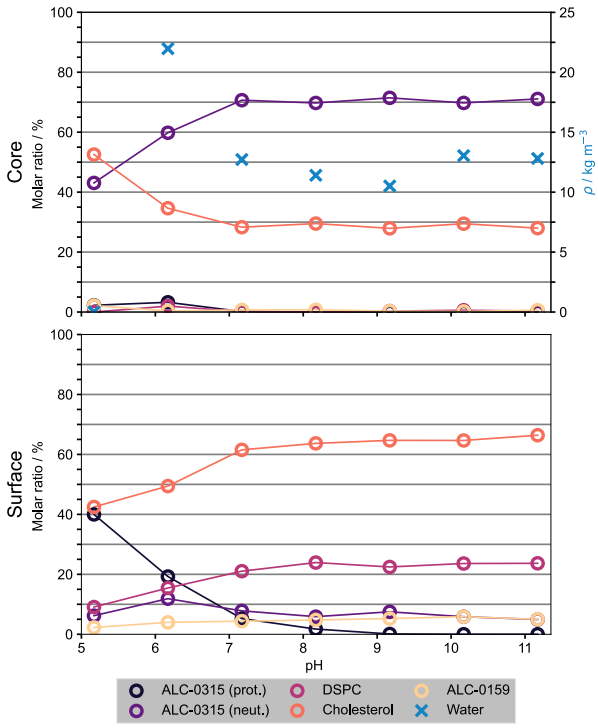

Fig. 3 Lipid distribution within LNPs. Molar ratios of lipids within both the core (top panel) and the lipid surface (bottom panel) of the LNP-mimetic systems as a function of pH are shown. Additionally shown is the mass density of water (*blue*, top panel) within the LNP core. A molecule was assigned to the core if its selected atom was more than 1.8 nm below the LNP surface. The following atoms were selected for each molecule type: nitrogen for ALC-0315, phosphorus for DSPC, oxygen for cholesterol, nitrogen for ALC-0159, and oxygen for water. For details on the analyzed segments of the simulations, refer to the caption of Fig. 2.

simulations provide unprecedented insight into the protonation characteristics and structural organization of the LNP formulation, even under near-physiological pH conditions. Already at pH 6, over 70% of the aminolipids are deprotonated compared to 12% at pH 5, initiating a phase transition characterized by increased membrane thickness as deprotonated aminolipids migrate into the membrane core. This shift reduces the number of protonated aminolipids at the membrane/solvent interface while increasing the density of deprotonated aminolipids within the membrane core

(Fig. 2b). Among the helper lipids, DSPC and the PEGylated lipids (ALC-0159) preferentially remain at the membrane surface (see Fig. 2b). Occasionally, a few molecules transiently integrate into the membrane core, likely due to favorable interactions with aminolipids during structural rearrangement. The PEGylated lipids may stabilize hydrophobic defects and facilitate the positioning of neutral aminolipids at the membrane surface [18].

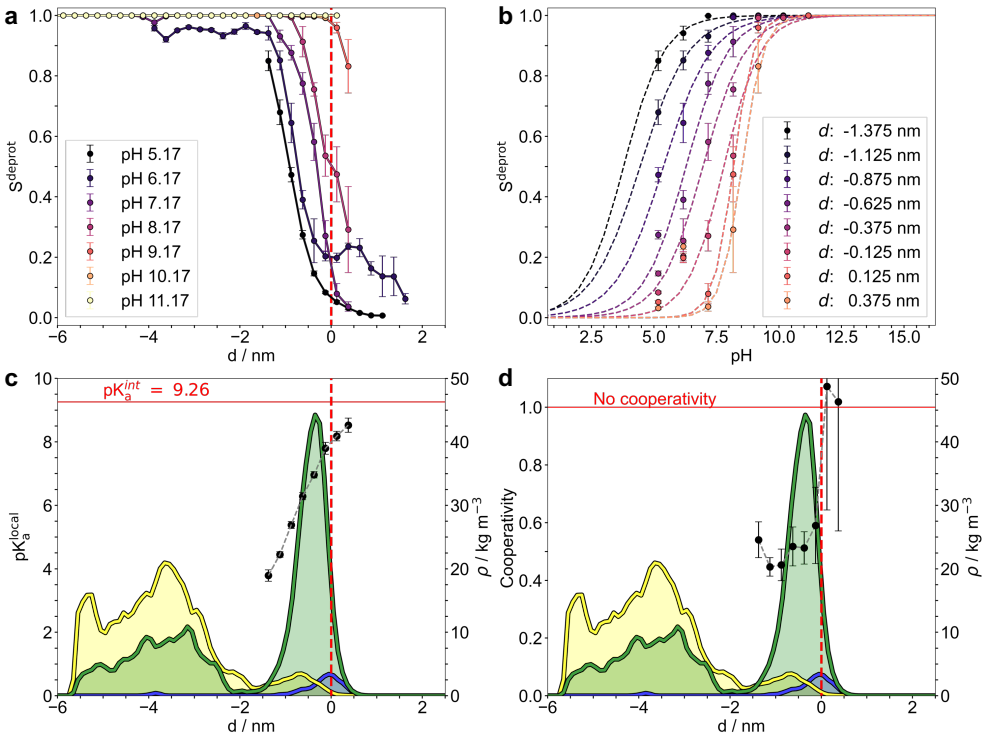

Fig. 4 Position-dependent pK$_a$ of aminolipids. a Fraction of deprotonated ALC-0315 aminolipids (S^{deprot}) at different pH values, plotted as a function of their distance from the median z-position of DSPC phosphorus atoms, averaged over both leaflets. Negative bin centers indicate titratable sites within the membrane, while positive bin centers correspond to sites above the membrane surface. Error bars respresent the standard error of the mean calculated via block averaging [36]. **b** Local titration curves for ALC-0315 within the membrane patch, showing S^{deprot} values averaged over both leaflets. Dashed lines represent fits to the generalized Henderson-Hasselbalch equation (see Eq. 5). Bins with fewer than 3 values or distances below $z = -1.5\,\mathrm{nm}$ were excluded. Error bars respresent the standard error of the mean calculated via block averaging [36]. **c** Local apparent pK$_a$ values (pK$_a^{\mathrm{local}}$) as a function of distance from the membrane surface, and **d** Cooperativity parameter (n) from Eq. 5, plotted against the distance to the membrane surface. Error bars respresent one standard deviation [37]. Additionally shown are the lipid densities at pH 7.17 for cholesterol (*green*), deprotonated (*yellow*), and protonated aminolipids (*blue*). For details on the analyzed segments of the simulations, refer to the caption of Fig. 2.

Position-dependent $\mathbf{pK_a}$ of aminolipids. The protonation states of aminolipids are strongly influenced by their insertion depth within the LNP-mimetic membrane (Fig. 1b). As shown in Fig. 4a, the fraction of deprotonated aminolipids (S^{deprot}) varies significantly with insertion depth (bin width of 0.25 nm) at different pH values. Aminolipids located near the surface of the monolayers ($d \approx 0$, defined as the distance from DSPC phosphorus atoms) exhibit substantially higher protonation levels (lower S^{deprot}) compared to those embedded in the LNP core phase ($d < 0$, Fig. 4b). This indicates that protonation is more favorable near the solvent-lipid interface. Notably, even at pH values around 8, well above the apparent $\mathrm{pK_a}$ (Fig. 1a), a significant fraction of surface aminolipids remains protonated.

The curves of S^{deprot} as a function of insertion depth (Fig. 4a) obtained from CpHMD simulations at different pH levels were transformed into pH-dependent titration curves at different insertion depths (Fig. 4b). This allowed for the determination of *local apparent pK_a* ($\mathrm{pK_a^{local}}$) values and *local degrees of cooperativity* using the generalized Henderson-Hasselbalch equation (Eq. 5), with results shown as *bullets* in Fig. 4c+d.

The apparent $\mathrm{pK_a^{local}}$ ranges between 6.5 and 8 at the monolayer surface of the LNP-mimetic, nearing the intrinsic $\mathrm{pK_a}$ of ALC-0315 in pure solvent (*red line* in Fig. 4c). This surface $\mathrm{pK_a^{local}}$ is significantly higher than the global apparent $\mathrm{pK_a}$ of the LNP. However, at an insertion depth of $d = -1.375$ nm, within the cholesterol-depleted region, the local $\mathrm{pK_a}$ drops sharply to approximately 4. This local dependence of the $\mathrm{pK_a}$ is further reflected in the mass density profiles of the aminolipids at pH 7.17 (Fig. 4c+d): These indicate a preference for the protonated state of ALC-0315 at the surface, but show a higher density of deprotonated aminolipids closer to the core of the LNP-mimetic membrane patch ($d < -1.8$ nm).
The cooperativity parameter n highlights anti-cooperativity in the LNP-mimetic, with reduced cooperativity near the membrane surface ($n \approx 1$) and enhanced cooperativity within the hydrophobic core, where n approaches 0.5 (Fig. 4d). This variation reflects the differences in electric shielding (relative permittivity) of surface and core regions of the LNP-mimetic.

Interactions between mRNA and lipids. To investigate the impact of mRNA on aminolipid protonation behavior and the spatial distribution of lipids and mRNA, we additionally performed CpHMD simulations at neutral pH of LNP-mimetic systems incorporating mRNA strands.

Figure 5 presents equilibrated snapshots of LNP-mimetic systems containing four mRNA strands, each with 20 nucleotides, after 1.5 μs of CpHMD simulation at pH 7, reflecting the N/P ratio of the *Comirnaty* formulation. The starting structures for these simulations were derived from microsecond constant-protonation simulations [18] (details in Methods section).
In contrast to mRNA-free systems, CpHMD simulations reveal a substantial presence of protonated aminolipids and water molecules within the LNP core at neutral pH (Fig. 5a). These protonated aminolipids localize near the negatively charged mRNA strands (Supplementary Fig. 9), forming polar cavities within the hydrophobic LNP core. These cavities, enriched with water and cations (Na^+), maintain the overall

LNP structure, characterized by a hydrophobic core surrounded by lipid monolayers (Fig. 5b).

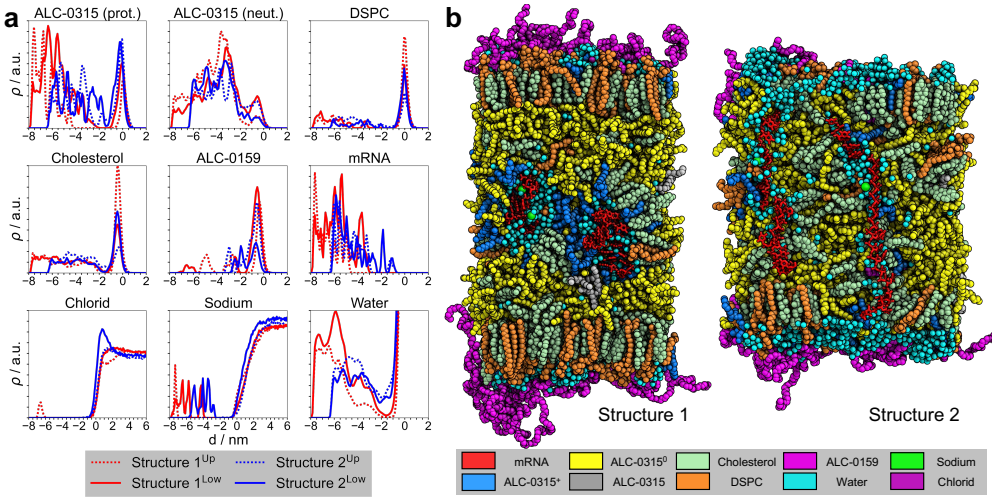

Fig. 5 Comirnaty LNP containing mRNA. a Average mass densities of all molecule types relative to the membrane surface, defined by the median z-position of the phosphorus atoms in DSPC in one leaflet, for two different mRNA configurations (Structure 1: Coil, Structure 2: Elongated) inside the LNP core at pH 7.17. The density curves were calculated using the following atoms for each molecule type: nitrogen for ALC-0315, phosphorus for DSPC, oxygen for cholesterol, nitrogen for ALC-0159, oxygen for water, and phosphorus for mRNA. **b** Snapshots of two different mRNA (*red*) configurations (Structure 1: Coil, Structure 2: Elongated) inside the LNP-mimetic system at pH 7.17. The nucleotide strands are embedded within the lipid bulk phase and surrounded by water (*cyan*), protonated ALC-0315 (*blue*), DSPC (*orange*), cholesterol (*palegreen*), sodium ions (*green*), and chloride ions (*purple*). Deprotonated ALC-0315 (*yellow*) is depleted around the nucleotides. The remaining helper lipids, protonated ALC-0315, and ALC-0159 (*hot pink*) are located at the surface facing towards the polar solvent. ALC-0315 without a specific protonation state ($0.2 \leq \lambda \leq 0.8$) is shown in *gray*. Densities were averaged after convergence of box vectors.

Discussion

Previous MD studies of LNP structure and dynamics have predominantly relied on fixed protonation states for titratable aminolipids, guided by the experimentally determined apparent pK_a values of ≈ 6 for complete lipid nanoparticles. These estimates differ substantially from the intrinsic pK_a of aminolipids (≈ 9), that may be derived from NMR measurements of water-soluble aminolipid analogs [11].
In this work, we investigated the molecular organization of LNP core and shell structures using atomistic constant-pH MD simulations, enabling dynamic adjustment of aminolipid protonation states in response to local environmental conditions. By treating pH as an adjustable parameter alongside the intrinsic pK_a, our simulations captured unbiased distributions of aminolipid protonation for systems containing hundreds of titratable sites. These simulations spanned a physiologically relevant pH range (5–11) and provided atomistic insights into the structural and protonation dynamics of LNP-mimetic systems. The use of CpHMD is well justified, given the absence of a pH gradient between the LNP core and the external environment [41, 42].

Increasing the pH significantly impacts both the average protonation state and the spatial distribution of aminolipids, driving a phase transition from a bilayer-like structure at acidic pH (pH 5) to an LNP-mimetic configuration at neutral or basic pH ≥ 7. This transition results in a hydrophobic core flanked by two polar monolayers (Fig. 2a). Similar accumulation of deprotonated aminolipids, along with cholesterol, at higher pH within the core of LNP-mimetic systems has been observed in constant-protonation MD simulations [18, 24], where all aminolipids were assumed to be fully deprotonated. However, this assumption corresponds to an unrealistically high pH > 9 (see Supplementary Fig. 6), beyond the physiologically relevant range. Assuming a constant ratio for the area per volume for LNP-mimetic systems [18] and full spherical LNPs, CpHMD simulations yield LNP diameters for mRNA-free LNPs of $39-42$ nm (for pH ≥ 8) and of $47-52$ nm for *Comirnaty* LNPs including mRNA (4,000 nucleotides) at neutral pH.

The CpHMD simulations reveal that the phase transition is closely tied to a redistribution of core and shell lipid compositions. As pH increases, deprotonated aminolipids preferentially localize within the core, while the cholesterol ratio within the core decreases to $\approx 30\%$ at neutral pH. Concurrently, cholesterol accumulates within the polar shell, reaching $> 60\%$, which is close to its solubility limit in phospholipid membranes (66 % in PC bilayers [40]). Notably, even at neutral pH 7, the lipid monolayers surrounding the core retain a significant fraction of protonated aminolipids ($\approx 5\%$, shown in *blue* in Fig. 3). It is important to note that artificial restraints on the simulation system may impede the phase transition between low and neutral or basic pH values [43].

The constant-pH approach enabled the unbiased determination of the *apparent* pK_a of aminolipids within the LNP-mimetic system to 5.71 ± 0.01, representing a significant decrease by ≈ 3.5 pK_a units compared to the intrinsic pK_a of the *Comirnaty* aminolipid in solvent. This value closely aligns with the experimentally measured pK_a of *Comirnaty* LNPs of 6.09 [44]. Similar shifts by 2-3 units relative to intrinsic pK_a values have also been reported for other mRNA LNPs based on different aminolipids

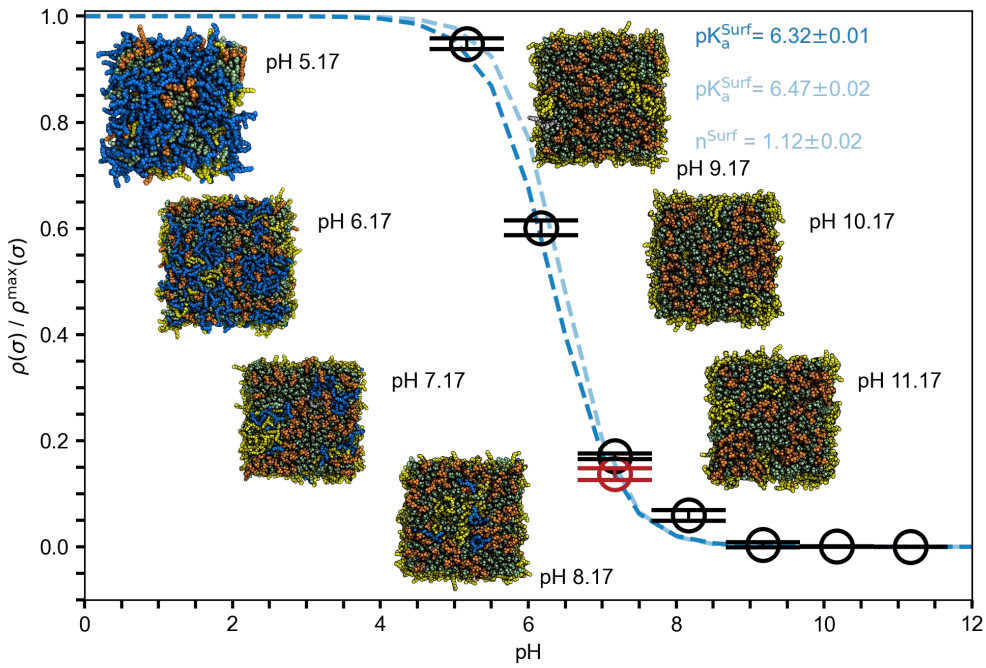

Fig. 6 pH-dependent surface charge density of LNP-mimetic systems. The calculation included only protonated ALC-0315 aminolipids within 1.8 nm of, or above, the median position of the DSPC phosphorus atoms in one leaflet. The number of protonations was divided by the respective box area. Charge densities were then averaged over both leaflets in every frame. Error bars represent the standard error of the mean, calculated via block averaging [36]. The charge density for a system containing mRNA (Structure 1) is shown in *red*. The values were normalized by the maximal charge density, $\rho^{\max}(\sigma)$, derived from constant-protonation simulations with all aminolipids protonated [18]. For details on the analyzed segments of the simulations, refer to the caption of Fig. 2.

such as D-Lin-DMA-MC3 [11]. Noteworthy, a simplified approach that analyzed the potential of mean force (PMF) of the aminolipid studied as a function of distance from the center of the membrane reached a smaller shift of $\Delta \mathrm{pK_a} \approx 2.5$ for the same aminolipid (ALC-0315) [35]. However, the latter approach neglects any phase changes of the membrane upon protonation of aminolipids and thus does not yield the titration curve for the full LNP system.

Importantly, the experimental $\mathrm{pK_a}$ value was derived from TNS binding assays, which measure fluorescence changes due to interactions between TNS and charged aminolipids at the LNP surface. Carrasco *et al.* [11] observed that apparent $\mathrm{pK_a}$ values determined via TNS binding assays tend to be higher than those obtained from ζ-potential measurements. Consistent with this, the apparent $\mathrm{pK_a}$ calculated from the LNP *surface charge* in the CpHMD simulations (Fig. 6) is approximately 0.5 units higher than the $\mathrm{pK_a}$ derived from the aminolipid protonation ratio. Therefore, we anticipate that the apparent $\mathrm{pK_a}$ of ALC-0315 would fall below 6 when determined via ζ-potential measurements.

The apparent pK_a of approximately 5.7 for aminolipids of the LNP-mimetic system was further analyzed depending on the aminolipid insertion depth. The results revealed significantly reduced pK_a^{local} values within the hydrophobic core and an apparent pK_a^{local} close to the intrinsic value at the polar LNP surface. This observation is particularly relevant because the experimental pK_a of 6.09 implies that roughly 90% of aminolipids are deprotonated at pH 7. In contrast, the CpHMD simulations indicate that about 50% of surface aminolipids remain protonated in (mRNA-devoid) LNP-mimetic systems. These findings align with those of Carrasco *et al.* [11], who reported that various aminolipid-based LNPs exhibit a positive ζ-potential near their apparent pK_a.

The CpHMD simulations of LNP-mimetic systems incorporating mRNA provide further evidence supporting the hypothesis that polynucleotides elevate the local pK_a of aminolipids, thereby enhancing their protonation within the LNP core [18]. This result diverges from the hypothesis proposed by Szebeni *et al.*[42], which suggests that negatively charged mRNA is primarily stabilized within an apolar LNP core through hydrogen bonding with deprotonated aminolipids. Instead, the mRNA-lipid arrangement observed in our simulations more closely aligns with the model proposed by Yanez-Arteta *et al.* [45], in which mRNA is encapsulated in a cylindrical configuration within the LNP and surrounded by an aqueous environment. Overall, approximately 80% of all aminolipids were deprotonated (S^{deprot}) in the mRNA-containing systems (Fig. 5) at pH 7.17. This corresponds to a shift of the overall apparent pK_a by approximately one unit (see Fig. 1a, additional data point marked in *black*). However, in turn, the pK_a analyzed based on the LNP surface charge is hardly affected by the presence of mRNA (Fig. 6, data point marked by *red* circle).

Conclusion

This study provides atomistic insights into the pH-dependent behavior and structural dynamics of LNP-mimetic systems, focusing on aminolipid protonation and its implications for lipid organization and mRNA interaction. By employing scalable constant-pH MD simulations [34], we reveal how environmental factors influence the protonation state and distribution of aminolipids, driving highly cooperative structural transitions within the LNP. Our findings bridge the gap between experimentally observed macroscopic properties, such as apparent pK_a values, and the underlying molecular mechanisms governing LNP functionality. Furthermore, the comparison with experimental data validates our computational approach and underscores the utility of CpHMD simulations in elucidating the intricate interplay between lipid and nucleic acid components.

Our results on the localization and protonation behaviors of aminolipids within the LNP core and shell provide a solid foundation for the rational design of next-generation LNP formulations with enhanced stability, tunable pH responses, and improved therapeutic delivery efficiency. Future work will explore the role of different lipid types (acyl chain saturation, headgroup chemistry), including non-standard lipids, on the distribution and the local pK_a of aminolipids, and extend these approaches to study

the interactions of diverse cargo types, further advancing our understanding of LNP systems in biomedical applications.

Methods

Force field parameters for ALC-0315 (prot/neut) and ALC-0159. Force field parameters for ALC-0315 and ALC-0159 were retrieved from the CHARMM General Force Field (CGenFF v4.6) [46] with the CGenFF program (v3.0) [47–49]. The partial charges of the atoms within the acyl chains, PEG monomers, ester bonds, and hydroxyl groups were manually set to default values of CGenFF [46] and the CHARMM force field for lipids [50]. For the titratable group in the aminolipid, the partial charges used for both the protonated (charge: +1.0) and the deprotonated (charge: 0.0) state were assigned by the CGenFF program [47]. In the protonated state, a remaining charge of 0.003 e was added to the proton resulting in a total charge of $q^H = 0.323\,\mathrm{e}$. The partial charges in the linker region between the hydrophobic tails and the polymer of the PEG-ylated lipid were assigned based on the parameters for dimethylacetamide, which was already included in CGenFF (resname: DMA) [46]. Atom types or bonded potentials assigned by the CGenFF program [47–49] were not modified. Cholesterol and DSPC parameters were taken from the CHARMM36 force field for lipids [50–52]. The July 2022 version of the CHARMM36 force field port for Gromacs was used for all simulations.

Constant-pH parameters for ALC-0315. The influence of the pH on a realistic LNP lipid formulation was studied using the recently published constant-pH code implemented in Gromacs by Aho *et al.* [34]. The algorithm uses λ-dynamics to interpolate between charges corresponding either to the protonated ($\lambda = 0$) or the deprotonated ($\lambda = 1$) state of each titratable group. The λ-dependent electrostatic potential $\Phi(\mathbf{R}_i, \lambda)$ on atom i is then defined as:

$$\Phi(\mathbf{R}_i, \lambda) = \sum_{j}^{n_{rest}} \frac{q_j}{4\pi\epsilon_0 r_{ij}} + \sum_{m}^{N_{sites}} \sum_{j}^{n_m} \frac{(1-\lambda_m)\cdot q_j^A + \lambda_m \cdot q_j^B}{4\pi\epsilon_0 r_{ij}}, \tag{1}$$

with n_{rest} as number of atoms not part of any titratable site; N_{sites} as number of titratable sites; and n_m as number of atoms part of a titratable site each with a partial charge of q_j. By interpolating partial charges instead of potential energy functions, the computational overhead is significantly reduced, allowing the simulation of hundreds of titratable sites within the same system [34]. Here, the LNP-mimetic systems typically contain 488 titratable aminolipids (see Table 1). Additionally, three λ-dependent potential energy functions are added to the total Hamiltonian of the system: the correction potential ($V^{MM}(\lambda)$), the biasing potential ($V^{bias}(\lambda)$), and the pH-dependent potential ($V^{pH}(\lambda)$)[34]. The terms $V^{bias}(\lambda)$ and $V^{pH}(\lambda)$ are analytical functions that are described in more detail in Aho *et al.* [34]. If not otherwise specified, the simulations in this paper applied a biasing potential $V^{bias}(\lambda)$ with a barrier height of 7.5 kJ mol^{-1}, corresponding to the default value set by pHbuilder [53]. The correction potential $V^{MM}(\lambda)$ is defined as the negative of the deprotonation free energy,

$$V^{MM}(\lambda) = -\Delta G^{MM}(\lambda). \tag{2}$$

The implementation of Aho *et al.* [34] uses a polynom to represent $V^{MM}(\lambda)$. We employed the workflow described by Buslaev *et al.* [54] and Jansen *et al.* [53] to derive the *a priori* unknown polynomial coefficients via thermodynamic integration. The modified Gromacs version [34] and the pHbuilder tool (v1.2.4/5) [53] were used to generate all relevant structural and initial topology files for the parameterization. For the thermodynamic integration (system A), a single aminolipid was initially placed in a 6x6x6 nm^3 box solvated with water, one counter ion, and an additional salt concentration of 150 mM Na^+Cl^-. During the simulation, position restraints were applied to avoid strong interactions between the aminolipid and the buffer particle. The potential energy of the initial structure was minimized using the steepest descent algorithm until a tolerance of 1,000 kJ mol^{-1} nm^{-1} or a maximum of 5,000 steps was reached (maximum step size: 0.01 nm). Following energy minimization, the system was equilibrated in the NVT ensemble for 100 ps, and subsequently in the NPT ensemble for 900 ps, using the leap-frog integrator with a time step of 0.001 ps and 0.002 ps, respectively. The equilibrated structure then served as the initial configuration for the different λ windows. No initial velocities were generated at the start of the simulation.

In general, temperature and pressure were maintained in all simulations using the velocity-rescale algorithm [55] (T^{ref}=310 K and $\tau_T = 0.5$ ps) and the C-rescale algorithm [56] (p^{ref}=1 bar, $\tau_P = 5.0$ ps, and a compressibility of 4.5×10^{-5} bar^{-1}), respectively. Both quantities were coupled with a frequency of 20 steps. According to the recommendations of Kim *et al.* [57] the automated buffer setting was overridden (Verlet-buffer-tolerance = -1) and the outer cut-off distance for the short-range neighbor list (rlist) was set to 1.35 nm with a frequency of 20 steps to update the neighbor list (nstlist). Forces from van der Waals interactions were smoothly switched to 0 between 1.0 nm and 1.2 nm (inner cut-off distance). Electrostatic interactions were handled using the fast smooth Particle-Mesh Ewald (PME) method [58] with a real-space cut-off distance of 1.2 nm and a Fourier spacing of 0.14 nm. Bonds including hydrogen atoms, were constrained and handled with the LINCS algorithm [59].

For system A (see Tab. 1), the average minimum distance between all atoms in the aminolipid and the buffer particle was 3.54 nm, with the distances ranging from a minimum of 2.48 nm to a maximum of 4.34 nm. Contributions from the three constant-pH specific potentials $V^{MM}(\lambda)$, $V^{bias}(\lambda)$, and $V^{pH}(\lambda)$, are not considered during the thermodynamic integration simulations. Averages of $\frac{\delta V}{\delta \lambda}$ were sampled for λ values between -0.10 and 1.10 with an equidistant spacing of 0.05 λ, and a temporal output frequency of 1 ps. Estimates of $\langle \frac{\delta V}{\delta \lambda} \rangle$ were calculated from the entire simulation length of 600 ns per λ window. Convergence of the estimate was checked by monitoring the value of $\langle \frac{\delta V}{\delta \lambda} \rangle$ over time (see Supplementary Fig. 1a). Polynomial coefficients were then fitted with the *fit_parameterization.py* script provided by pHbuilder [53] (see Supplementary Fig. 1b). For the aminolipid, a one-dimensional polynom of order 8 was used to fit $\frac{\delta V}{\delta \lambda}$.

The quality of the fitted parameters was assessed by running 10 independent simulations (system B, Tab. 1) without position restraints and without contributions from $V^{bias}(\lambda)$ and $V^{pH}(\lambda)$ (i.e., pH = pK_a). The initial structure of a single aminolipid in solvent was first minimized and then equilibrated for each replica simulation, using

the three-step protocol described above. Initial velocities were not generated for the replica simulations. The distribution of λ should then follow an uniform distribution under these conditions if a proper estimate of $\langle \frac{\delta V}{\delta \lambda} \rangle$ is provided [34, 53, 54] (see Supplementary Fig. 2).
We further evaluated our estimated parameters by performing titration simulations (system C, Tab. 1) in the pH range of 5.17 to 11.67 with increments of 0.5 pH units. In these simulations, all correction potentials ($V^{MM}(\lambda)$, $V^{bias}(\lambda)$, and $V^{pH}(\lambda)$) were applied, with the pH gradually increasing. A single aminolipid was placed in solvent with a physiological salt concentration of 150 mM. The structure was first minimized and then equilibrated again using the three-step protocol described above. The equilibrated structure then served as the initial configuration for all subsequent simulations. Initial velocities were not generated for the replica simulations. We performed 9 replica simulations per pH value, each with a duration of 700 ns. Systems were set up using the *create_titration.py* script provided by pHbuilder [53]. Unless otherwise specified, the buffer parameters from Buslaev *et al.* [54] were used.

Multi-component systems

Lipid-Only Systems. The CpHMD simulations of the lipid composition of *Comirnaty* LNPs were started from an equilibrated snapshot at low pH previously obtained in classical MD simulations using a fixed protonation for the aminolipids [18]. The snapshot was taken after 4 μs of an all-atom simulation. The molar lipid ratio for ALC-0315:DSPC:cholesterol:ALC-0159 (PEGylated lipid) is 46.3:9.4:42.7:1.6, corresponding to 122 aminolipids, 24 DSPC molecules, 112 cholesterol molecules, and 6 ALC-0159 (PEGylated lipids) in system D-E (see Table 1).

Prior to starting the CpHMD simulations, an energy minimization was performed, with a maximum step of 0.0001 nm, an energy tolerance of 1,000 kJ mol^{-1} nm^{-1}, and a maximum of 5,000 steps. Only aminolipids were allowed to change their protonation states, while standard force field parameters were used for the remaining lipids. Titration of the lipid composition was performed in the range from 5.17 . . . 11.17 with a step size of 1 pH unit. To probe the influence of different buffer particle concentrations and different initial protonation states of the lipids, we repeated the titration for two different initial states (system D, E, Tab. 1). In system D, 245 buffer atoms were added with all lipids starting from a protonated state. The number of buffer atoms equals $2 \cdot N + 1$ with N representing the number of titratable residues in the system. In system E, 123 buffer atoms were added with only half of the lipids starting from a protonated state. Simulations ran for a minimum of 1 μs. After the simulations were completed, the box vectors (Supplementary Fig. 3) and the number of (de)protonated aminolipids (Supplementary Fig. 4a) were compared between systems D and E. No significant differences were observed in these quantities across different buffer particle concentrations and pH levels. However, at pH 6.17, which is close to the apparent pK_a, the membrane surface area decreased more rapidly in system D (higher buffer concentration).

Simulations of system D (see Tab. 1) that showed significant structural changes were replicated twice in x/y direction (system $F^{1\text{-}6}$, Tab. 1). Bulk water was further removed to prevent large computational overheads. Remaining ion numbers were adapted to keep the ion concentration comparable between systems. Protonation states of the aminolipids from the last snapshot of the simulations were used as initial states for the enlarged membranes. Protonation was assigned if the λ coordinate was below a value of 0.2. Unfortunately, the actual version of the cpHMD implementation does not allow to assign different initial protonation states to the same group of residues. Therefore, we introduced a new residuetype (BLCP, $\lambda^{init} = 1$) as an exact copy of the aminolipid residuetype (ALCP, $\lambda^{init} = 0$) that only differs in its initial protonation state. The amount of buffer atoms was reduced to 60 particles per system based on a preliminary estimation of the charge fluctuation at pH 7.17. An energy minimization (steepest descent) with a maximum step size of 0.01 nm, an energy tolerance of 1,000 kJ mol^{-1} nm^{-1}, and a maximum of 30 steps was performed before starting the simulation. Systems at pH 6.17 and pH 7.17 became unstable twice, first after 0.9 μs and 1 μs, and then again after an additional 1.1 μs and 2.0 μs. This instability occurred when the λ-coordinate of the buffer exceeded the maximum threshold of 1.15, indicating significant changes in the protonation state of the aminolipids during the simulation (see Supplementary Fig. 7b). The issue was resolved by restarting the simulation from a later snapshot, initializing the protonation states based on the corresponding λ-coordinates ($\lambda < 0.2$, protonated), and adjusting the number of counterions. Prior to restarting the simulation, a short energy minimization (steepest descent) was performed, with a maximum of 30 steps and an energy tolerance of 1,000 kJ mol^{-1} nm^{-1} (maximum step 0.01 nm). After the second restart, the number of buffer particles in these systems was increased to 90. Tab. 1 shows the final molecule numbers for systems $F^{1,2}$. The mass density profiles shown in Supplementary Fig. 8 indicate that the buffer particles avoid the hydrophobic interior of the membranes.

Lipid/mRNA Systems. To investigate the impact of mRNA on the protonation state of ALC-0315 within the LNP core, two equilibrated snapshots of mRNA-lipid simulation systems, previously published by Trollmann and Böckmann [18], were used as initial structures. These structures contained four strands of negatively charged poly-nucleotides encapsulated within the lipid-bulk phase and included a mix of (constantly) deprotonated and protonated aminolipids. Notably, the mRNA strands differ in structure between the two systems due to the random self-assembly process used to generate the systems [18]. The constant protonation states in these snapshots were taken as initial protonation states of the aminolipids in the CpHMD simulations to preserve the pre-equilibrated interaction network between mRNA and lipids as much as possible. After adding the buffer particles, an energy minimization with a maximum step size of 0.01 nm, an energy tolerance of 1,000 kJ mol^{-1} nm^{-1}, and a maximum of 30 steps was performed before starting the simulation. Both systems (system G, Tab. 1) were simulated with a pH of 7.17. Parameters for the (modified) mRNA nucleotides were taken from the CHARMM36 force field [60, 61].

Analysis of the constant-pH trajectories

The analysis of the titratable groups follows the recommendations outlined by Aho *et al.* [34]. The fraction of deprotonated aminolipids (S^{deprot}) per frame was computed by

$$S^{deprot}(pH) = \frac{N^{deprot}}{N^{prot} + N^{deprot}} \ , \tag{3}$$

where N^{prot} and N^{deprot} refer to the total number of (de-)protonated sites. A single site is considered protonated if its λ-coordinate is below 0.2, and deprotonated if λ is above 0.8.
If a single-molecule system was simulated for different pH values, the $\mathrm{pK_a}$ was determined by fitting the Henderson-Hasselbalch equation to the values of S^{deprot}:

$$S^{deprot}(pH) = \frac{1}{10^{(pK_a - pH)} + 1} \ . \tag{4}$$

For systems containing multiple titratable sites the $\mathrm{pK_a}$ was additionally determined from a fit to the generalized Henderson-Hasselbalch equation originally used for titration curves of polymeric acids [39]:

$$S^{deprot}(pH) = \frac{1}{10^{[n \cdot (pK_a - pH)]} + 1} \ , \tag{5}$$

the coefficient n was interpreted in this work as a measure of the cooperativity for the protonation within a system of several aminolipids. A value $n < 1$ refers to negative cooperativity, or anti-cooperativity, while $n > 1$ indicates positive cooperativity between the titratable sites. The same function was used by Carrasco *et al.* [11] to fit titration curves of LNPs obtained from ζ-potentials.

Data availability

All simulation models, input files, and structures will be made available in a separate Zenodo repository after final acceptance of the manuscript.

Acknowledgements

The authors gratefully acknowledge the scientific support and HPC resources provided by the Erlangen National High Performance Computing Center (NHR@FAU) of the Friedrich-Alexander-Universität Erlangen-Nürnberg (FAU). The hardware is funded by the German Research Foundation (DFG).

Competing interests

The authors declare no competing interests.

Additional information

The supplementary material includes

- Supplementary Figures 1 – 9

References

[1] Akinc, A. *et al.* The Onpattro story and the clinical translation of nanomedicines containing nucleic acid-based drugs. *Nat. Nanotechnol.* **14**, 1084–1087 (2019).

[2] Polack, F. P. *et al.* Safety and efficacy of the BNT162b2 mRNA Covid-19 vaccine. *N. Engl. J. Med.* **383**, 2603–2615 (2020).

[3] Baden, L. R. *et al.* Efficacy and safety of the mRNA-1273 SARS-CoV-2 vaccine. *N. Engl. J. Med.* **384**, 403–416 (2021).

[4] Kremsner, P. G. *et al.* Efficacy and safety of the CVnCoV SARS-CoV-2 mRNA vaccine candidate in ten countries in europe and latin america (HERALD): a randomised, observer-blinded, placebo-controlled, phase 2b/3 trial. *Lancet Infect. Dis.* **22**, 329–340 (2022).

[5] Stadler, C. R. *et al.* Preclinical efficacy and pharmacokinetics of an RNA-encoded T cell-engaging bispecific antibody targeting human claudin 6. *Sci. Transl. Med.* **16**, eadl2720 (2024).

[6] O'Brien, Z. *et al.* A novel lipid nanoparticle (NBF-006) encapsulating glutathione S-transferase P (GSTP) siRNA for the treatment of KRAS-driven non-small cell lung cancer. *Cancer Res* **78**, 5917–5917 (2018).

[7] Hayashi, C. T. H. *et al.* mRNA-LNP expressing PfCSP and Pfs25 vaccine candidates targeting infection and transmission of plasmodium falciparum. *NPJ Vaccines* **7**, 155 (2022).

[8] Chuang, Y.-M. *et al.* A mosquito AgTRIO mRNA vaccine contributes to immunity against malaria. *NPJ Vaccines* **8**, 88 (2023).

[9] Escalona-Rayo, O. *et al.* In vitro and in vivo evaluation of clinically-approved ionizable cationic lipids shows divergent results between mRNA transfection and vaccine efficacy. *Biomed. Pharmacother.* **165**, 115065 (2023).

[10] Schoenmaker, L. *et al.* mRNA-lipid nanoparticle COVID-19 vaccines: Structure and stability. *Int. J. Pharm.* **601**, 120586 (2021).

[11] Carrasco, M. J. *et al.* Ionization and structural properties of mRNA lipid nanoparticles influence expression in intramuscular and intravascular administration. *Commun. Biol.* **4**, 956 (2021).

[12] Maurer, N. *et al.* Spontaneous entrapment of polynucleotides upon electrostatic interaction with ethanol-destabilized cationic liposomes. *Biophys. J.* **80**, 2310–2326 (2001).

[13] Evers, M. J. W. *et al.* State-of-the-art design and rapid-mixing production techniques of lipid nanoparticles for nucleic acid delivery. *Small Methods* **2**, 1700375 (2018).

[14] Semple, S. C. *et al.* Efficient encapsulation of antisense oligonucleotides in lipid vesicles using ionizable aminolipids: formation of novel small multilamellar vesicle structures. *Biochim. Biophys. Acta* **1510**, 152–166 (2001).

[15] Ge, X., Chen, L., Zhao, B. & Yuan, W. Rationale and application of PEGylated lipid-based system for advanced target delivery of siRNA. *Front. Pharmacol.* **11**, 598175 (2020).

[16] Mui, B. L. *et al.* Influence of polyethylene glycol lipid desorption rates on pharmacokinetics and pharmacodynamics of siRNA lipid nanoparticles. *Mol. Ther. Nucleic Acids* **2**, e139 (2013).

[17] Kulkarni, J. A., Witzigmann, D., Leung, J., Tam, Y. Y. C. & Cullis, P. R. On the role of helper lipids in lipid nanoparticle formulations of siRNA. *Nanoscale* **11**, 21733–21739 (2019).

[18] Trollmann, M. F. W. & Böckmann, R. A. mRNA lipid nanoparticle phase transition. *Biophys. J.* **121**, 3927–3939 (2022).

[19] Paramasivam, P. *et al.* Endosomal escape of delivered mRNA from endosomal recycling tubules visualized at the nanoscale. *J. Cell Biol.* **221** (2022).

[20] Hafez, I. M., Maurer, N. & Cullis, P. R. On the mechanism whereby cationic lipids promote intracellular delivery of polynucleic acids. *Gene Ther.* **8**, 1188–1196 (2001).

[21] Semple, S. C. *et al.* Rational design of cationic lipids for siRNA delivery. *Nat. Biotechnol.* **28**, 172–176 (2010).

[22] Ramezanpour, M. *et al.* Ionizable amino lipid interactions with POPC: implications for lipid nanoparticle function. *Nanoscale* **11**, 14141–14146 (2019).

[23] Park, S., Choi, Y. K., Kim, S., Lee, J. & Im, W. CHARMM-GUI membrane builder for lipid nanoparticles with ionizable cationic lipids and PEGylated lipids. *J. Chem. Inf. Model.* **61**, 5192–5202 (2021).

[24] Paloncýová, M., Čechová, P., Šrejber, M., Kührová, P. & Otyepka, M. Role of ionizable lipids in SARS-CoV-2 vaccines as revealed by molecular dynamics simulations: From membrane structure to interaction with mRNA fragments. *J.*

Phys. Chem. Lett. **12**, 11199–11205 (2021).

[25] Grava, M. *et al.* Combining molecular dynamics simulations and x-ray scattering techniques for the accurate treatment of protonation degree and packing of ionizable lipids in monolayers. *J. Chem. Phys.* **159** (2023).

[26] Čechová, P., Paloncýová, M., Šrejber, M. & Otyepka, M. Mechanistic insights into interactions between ionizable lipid nanodroplets and biomembranes. *J. Biomol. Struct. Dyn.* 1–11 (2024).

[27] Philipp, J. *et al.* pH-dependent structural transitions in cationic ionizable lipid mesophases are critical for lipid nanoparticle function. *Proc. Natl. Acad. Sci. U. S. A.* **120**, e2310491120 (2023).

[28] Leung, A. K. K. *et al.* Lipid nanoparticles containing siRNA synthesized by microfluidic mixing exhibit an electron-dense nanostructured core. *J. Phys. Chem. C Nanomater. Interfaces* **116**, 18440–18450 (2012).

[29] Unruh, T. *et al.* Mesoscopic structure of lipid nanoparticle formulations for mRNA drug delivery: Comirnaty and drug-free dispersions. *ACS Nano* **18**, 9746–9764 (2024).

[30] Paloncýová, M. *et al.* Atomistic insights into organization of RNA-loaded lipid nanoparticles. *J. Phys. Chem. B* **127**, 1158–1166 (2023).

[31] Kjølbye, L. R. *et al.* Martini 3 building blocks for lipid nanoparticle design. *ChemRxiv* (2024).

[32] Tesei, G. *et al.* Lipid shape and packing are key for optimal design of pH-sensitive mRNA lipid nanoparticles. *Proc. Natl. Acad. Sci. U. S. A.* **121**, e2311700120 (2024).

[33] Donnini, S., Tegeler, F., Groenhof, G. & Grubmüller, H. Constant pH molecular dynamics in explicit solvent with -dynamics. *J. Chem. Theory Comput.* **7**, 1962–1978 (2011).

[34] Aho, N. *et al.* Scalable constant ph molecular dynamics in GROMACS. *J. Chem. Theory Comput.* **18**, 6148–6160 (2022).

[35] Hamilton, N. B., Arns, S., Shelley, M., Bechis, I. & Shelley, J. C. Calculating apparent pka values of ionizable lipids in lipid nanoparticle. http://doi.org/10.26434/chemrxiv-2024-32z25 (2024). ChemRxiv.

[36] Hess, B. Determining the shear viscosity of model liquids from molecular dynamics simulations. *J. Chem. Phys.* **116**, 209–217 (2002).

[37] Vugrin, K. W., Swiler, L. P., Roberts, R. M., Stucky-Mack, N. J. & Sullivan, S. P. Confidence region estimation techniques for nonlinear regression in groundwater

flow: Three case studies. *Water Resources Research* **43** (2007).

[38] Ansell, S. M. & Du, X. Novel lipids and lipid nanoparticle formulations for delivery of nucleic acids. https://patents.google.com/patent/WO2017075531A1/en (2015). [Online; accessed 19-May-2024].

[39] Katchalsky, A. & Spitnik, P. Potentiometric titrations of polymethacrylic acid. *J. Polym. Sci.* **2**, 432–446 (1947).

[40] Huang, J., Buboltz, J. T. & Feigenson, G. W. Maximum solubility of cholesterol in phosphatidylcholine and phosphatidylethanolamine bilayers. *BBA - Biomembranes* **1417**, 89–100 (1999).

[41] Zhao, B. *et al.* Determination of the interior ph of lipid nanoparticles using a ph-sensitive fluorescent dye-based dna probe. *Biosens. Bioelectron.* **251**, 116065 (2024).

[42] Szebeni, J. *et al.* Insights into the structure of comirnaty covid-19 vaccine: A theory on soft, partially bilayer-covered nanoparticles with hydrogen bond-stabilized mrna–lipid complexes. *ACS Nano* **17**, 13147–13157 (2023).

[43] Garaizar, A. *et al.* Toward understanding lipid reorganization in RNA lipid nanoparticles in acidic environments. *Proc. Natl. Acad. Sci. U. S. A.* **121**, e2404555121 (2024).

[44] Hope, M. J. *et al.* Lipid nanoparticle formulations. World Patent WO-2018081480-A1 (2018).

[45] Yanez Arteta, M. *et al.* Successful reprogramming of cellular protein production through mRNA delivered by functionalized lipid nanoparticles. *Proc. Natl. Acad. Sci. U. S. A.* **115**, E3351–E3360 (2018).

[46] Vanommeslaeghe, K. *et al.* CHARMM general force field: A force field for drug-like molecules compatible with the CHARMM all-atom additive biological force fields. *J. Comput. Chem.* **31**, 671–690 (2010).

[47] SILCSBIO. Cgenff. https://cgenff.com (2023). Accessed: 2024-3-25.

[48] Vanommeslaeghe, K. & MacKerell, A. D., Jr. Automation of the CHARMM general force field (CGenFF) I: bond perception and atom typing. *J. Chem. Inf. Model.* **52**, 3144–3154 (2012).

[49] Vanommeslaeghe, K., Raman, E. P. & MacKerell, A. D., Jr. Automation of the CHARMM general force field (CGenFF) II: assignment of bonded parameters and partial atomic charges. *J. Chem. Inf. Model.* **52**, 3155–3168 (2012).

[50] Klauda, J. B. *et al.* Update of the CHARMM all-atom additive force field for lipids: validation on six lipid types. *J. Phys. Chem. B* **114**, 7830–7843 (2010).

[51] Pitman, M. C., Suits, F., Mackerell, A. D., Jr & Feller, S. E. Molecular-level organization of saturated and polyunsaturated fatty acids in a phosphatidylcholine bilayer containing cholesterol. *Biochemistry* **43**, 15318–15328 (2004).

[52] Lim, J. B., Rogaski, B. & Klauda, J. B. Update of the cholesterol force field parameters in CHARMM. *J. Phys. Chem. B* **116**, 203–210 (2012).

[53] Jansen, A., Aho, N., Groenhof, G., Buslaev, P. & Hess, B. phbuilder: A tool for efficiently setting up constant pH molecular dynamics simulations in GROMACS. *J. Chem. Inf. Model.* **64**, 567–574 (2024).

[54] Buslaev, P. *et al.* Best practices in constant pH MD simulations: Accuracy and sampling. *J. Chem. Theory Comput.* **18**, 6134–6147 (2022).

[55] Bussi, G., Donadio, D. & Parrinello, M. Canonical sampling through velocity rescaling. *J. Chem. Phys.* **126**, 014101 (2007).

[56] Bernetti, M. & Bussi, G. Pressure control using stochastic cell rescaling. *J. Chem. Phys.* **153**, 114107 (2020).

[57] Kim, H., Fábián, B. & Hummer, G. Neighbor list artifacts in molecular dynamics simulations. *J. Chem. Theory Comput.* **19**, 8919–8929 (2023).

[58] Darden, T., York, D. & Pedersen, L. Particle mesh ewald: An $N \log(N)$ method for Ewald sums in large systems. *J. Chem. Phys.* **98**, 10089–10092 (1993).

[59] Hess, B., Bekker, H., Berendsen, H. J. C. & Fraaije, J. G. E. M. LINCS: A linear constraint solver for molecular simulations. *J. Comput. Chem.* **18**, 1463–1472 (1997).

[60] Xu, Y., Vanommeslaeghe, K., Aleksandrov, A., MacKerell, A. D., Jr & Nilsson, L. Additive CHARMM force field for naturally occurring modified ribonucleotides: CHARMM potential energy function. *J. Comput. Chem.* **37**, 896–912 (2016).

[61] Denning, E. J., Priyakumar, U. D., Nilsson, L. & Mackerell, A. D., Jr. Impact of 2'-hydroxyl sampling on the conformational properties of RNA: Update of the CHARMM all-atom additive force field for RNA. *J. Comput. Chem.* **32**, 1929–1943 (2011).

Table 1 Systems studied with all-atom molecular dynamics simulations using the constant-pH method.

System	ALC-0315:DSPC:Chol:ALC-0159:mRNA	H_2O:Na^+:Cl^-:Buf	Sim. Time (μs)	pH	Replicas	Objective
A	1:0:0:0:0	6938:19:20:1	0.6	-	25	Thermodynamic Integration
B	1:0:0:0:0	6937:19:20:3	2.5	9.26	10	Goodness of polynomial coefficients
C	1:0:0:0:0	6937:19:20:3	0.7	5.17-11.67	14x9	Intrinsic pK_a
D	122:24:112:6:0	21660:58:180:245	1.0/5	5.17-11.17	7x1	Apparent pK_a
E	122:24:112:6:0	21782:58:119:123	1.0/2.5	5.17-11.17	7x1	Apparent pK_a
F^1	488:96:448:24:0	47958:130:287:90[1]	5.9	6.17	1	Apparent pK_a (2x2)
F^2	488:96:448:24:0	45122:122:171:90[1]	7.1	7.17	1	Apparent pK_a (2x2)
F^3	488:96:448:24:0	37315:101:137:60	7.7	8.17	1	Apparent pK_a (2x2)
F^4	488:96:448:24:0	40702:110:110:60	7.4	9.17	1	Apparent pK_a (2x2)
F^5	488:96:448:24:0	35871:97:97:60	7.9	10.17	1	Apparent pK_a (2x2)
F^6	488:96:448:24:0	34255:93:93:60	7.6	11.17	1	Apparent pK_a (2x2)
G	488:96:448:24:4	49512:120:148:60	1.5/1.5	7.17	2	Interaction with mRNA (2x2)

[a]Final number of solvent molecules.